

Numerical considerations for Lagrangian stochastic dispersion models: Eliminating rogue trajectories, and the importance of numerical accuracy

Brian N. Bailey

Received: 23 December 2015 / Accepted: 14 June 2016

1 **Abstract** When Lagrangian stochastic models for turbulent dispersion are
2 applied to complex atmospheric flows, some type of ad hoc intervention is
3 almost always necessary to eliminate unphysical behaviour in the numerical
4 solution. Here we discuss numerical strategies for solving the non-linear
5 Langevin-based particle velocity evolution equation that eliminate such un-
6 physical behaviour in both Reynolds-averaged and large-eddy simulation ap-
7 plications. Extremely large or ‘rogue’ particle velocities are caused when the
8 numerical integration scheme becomes unstable. Such instabilities can be elim-
9 inated by using a sufficiently small integration timestep, or in cases where the
10 required timestep is unrealistically small, an unconditionally stable implicit
11 integration scheme can be used. When the generalized anisotropic turbulence
12 model is used, it is critical that the input velocity covariance tensor be real-
13 izable, otherwise unphysical behaviour can become problematic regardless of
14 the integration scheme or size of the timestep. A method is presented to ensure
15 realizability, and thus eliminate such behaviour. It was also found that the nu-
16 merical accuracy of the integration scheme determined the degree to which the
17 second law of thermodynamics or ‘well-mixed condition’ was satisfied. Perhaps
18 more importantly, it also determined the degree to which modelled Eulerian
19 particle velocity statistics matched the specified Eulerian distributions (which
20 is the ultimate goal of the numerical solution). It is recommended that future
21 models be verified by not only checking the well-mixed condition, but perhaps
22 more importantly by checking that computed Eulerian statistics match the
23 Eulerian statistics specified as inputs.

24 **Keywords** Lagrangian stochastic dispersion models · Large-eddy simulation ·
25 Rogue trajectories · Turbulent dispersion

B. N. Bailey (✉)
United States Department of Agriculture - Agricultural Research Service
Corvallis, OR, 97330, USA
e-mail: bailebri@oregonstate.edu

1 Introduction

Langevin-based Lagrangian stochastic models have proven to be a practical method for describing the dispersion of particulates in many classes of turbulent flows. In flows with inhomogeneous velocity statistics, early workers found that isotropic Langevin-based models failed, as particles tended to accumulate in regions of low turbulent stress. Early heuristic work to remedy this problem began in the atmospheric boundary-layer community and involved adding a mean bias velocity to the Langevin equation, which worked well in cases of weakly inhomogeneous flow (Wilson et al, 1981; Legg and Raupach, 1982). The problem was later formalized by enforcing the requirement that the particle plume should satisfy the “well-mixed condition” (WMC; Thomson, 1984) or equivalently the “thermodynamic constraint” (Sawford, 1986). In either case, it was noted that an initially uniformly distributed particle plume should not un-mix itself in the absence of sources or sinks, or more precisely, entropy cannot decrease (i.e., the second law of thermodynamics). This is a crucial requirement for any model, as a model in which entropy decreases in time is generally not useful given that it does not tend toward a uniform equilibrium state in the absence of sources or sinks.

A rigorous theoretical solution to the “un-mixing” problem was devised concurrently by Thomson (1987) and Pope (1987), whose remedies were based on the notion that the Lagrangian dispersion models should satisfy their corresponding macroscopic Eulerian conservation equations, which clearly satisfy the second law of thermodynamics. Thomson (1987) used the Fokker-Planck equation to determine the proper coefficients in the Langevin equation, while Pope (1987) used the Navier-Stokes equations. The present paper primarily focuses on the Thomson approach because it is the most common in atmospheric applications (Lin et al, 2013), although similar problems are likely to arise when the Pope approach is used depending on the chosen form of the model.

Despite the fact that the Thomson model should satisfy the second law of thermodynamics in theory, authors have begun to report unphysical model behaviour, particularly in cases with complex inhomogeneity. This has been revealed by the failure of computed particle plumes to satisfy the WMC in practice (Lin, 2013), or by the presence of unrealistically large or ‘rogue’ particle velocities (Yee and Wilson, 2007; Postma et al, 2012; Wilson, 2013; Bailey et al, 2014; Postma, 2015). Although the Thomson model has been in use for several decades, it is only until recently that authors began explicitly acknowledging the unphysical behaviour in the numerical solutions of model equations.

Several methods have been suggested to deal with such unphysical behaviour. The simplest of which is ad hoc intervention in which velocities are artificially limited to some predetermined range. When a particle becomes rogue (according to some predefined criteria), the particle velocity is either artificially reset to some value, or the particle trajectory is restarted from the beginning. This method removes rogue velocities, but does not in general satisfy the second law of thermodynamics. Numerous discussions between the

author and colleagues using these types of models have revealed that some form of ad hoc intervention is ubiquitous, although rarely acknowledged in the literature. In some situations, relatively infrequent occurrence of rogue trajectories or some ad hoc correction may be tolerable, e.g., when only mean concentrations are desired. However, in other instances they may contaminate results to an unacceptable level (e.g., Postma et al, 2012; Wilson, 2013).

More advanced integration schemes have been suggested that reduce (although not eliminate) rogue velocities. Yee and Wilson (2007) formulated a semi-analytical integration scheme, whereby the integration is divided into analytical and numerical sub-steps. Unfortunately, certain conditions must be met in order to allow for the analytical sub-step, often requiring ad hoc intervention anyway when the conditions are not met. Bailey et al (2014) divided the integration into implicit and explicit sub-steps, which reduced but did not eliminate rogue trajectories. Lin (2013) presented a method that treats the turbulence field as stepwise homogeneous, which eliminates sharp local gradients that can cause numerical difficulties such as rogue trajectories. However, this method may be difficult to apply in cases of complex geometry and could require high grid resolution to resolve large gradients.

Authors have reported that reducing the timestep used in numerical integration of the Langevin equation could potentially reduce the frequency of rogue trajectories (e.g., Postma et al, 2012). It is probable that the timestep would have to be unfeasibly small to eliminate all rogue trajectories in complex flows. In accordance with this principle, Postma (2015) developed an adaptive timestep scheme that reduced the timestep based on the local turbulent time scales of the flow. This methodology still did not completely eliminate rogue trajectories, and would also be quite complex to apply in general three-dimensional flows.

The goal of the present study was to uncover the root cause of reported unphysical behaviour in certain Lagrangian stochastic dispersion models. A remedy for the problem was ultimately desired, which involved formulating a stable numerical scheme that satisfies the thermodynamic constraint and matches the Eulerian velocity statistics specified as inputs. The source code and input data for all examples presented herein are provided in the associated online material.

2 Reynolds-averaged Lagrangian stochastic models

In a Lagrangian framework, one can calculate the time evolution of particle position given information about the velocity field as

$$\frac{dx_{p,i}}{dt} = U_i + u_i, \quad (1)$$

where $x_{p,i}$ is particle position in Cartesian direction $i = (x, y, z)$, t is time, and U_i and u_i are respectively the mean and fluctuating particle velocity components.

Often in turbulent flows, only the ensemble-averaged component of $dx_{p,i}/dt$ is known, and the fluctuating component must be modelled. Thus, there has been large interest in developing practical models for the Lagrangian particle velocity fluctuations that can be driven by easily measured or estimated turbulence quantities such as the local turbulent kinetic energy. The unresolved Lagrangian velocity is commonly modelled using an analogy to Langevin (1908), who developed models for Brownian motion. The stochastic Langevin equation can be written in modern form as

$$du_i = -au_i dt + b_{ij} dW_j, \quad (2)$$

where dW is an increment in a Weiner process with zero mean and variance dt , and a and b are coefficients to be determined. This particular form assumes that the particle velocity is Markovian and Gaussian.

For homogeneous, isotropic turbulence, these coefficients can be determined independently such that u_i has the proper short- and long-time behaviour, which is made possible by the Markovian assumption. The b coefficient is commonly specified such that the small-time behaviour of u_i is consistent with Kolmogorov's second similarity hypothesis, which gives

$$b^2 dt = \langle (du_i)^2 \rangle = C_0 \bar{\epsilon} dt, \quad (3)$$

where $\langle \cdot \rangle$ is an ensemble average, C_0 is a 'universal' constant (Rodean, 1991; Du, 1997), and $\bar{\epsilon}$ is the mean dissipation rate of turbulent kinetic energy. The a coefficient is the inverse of the particle integral time scale τ_L , which is commonly assumed to be (c.f. Rodean, 1996)

$$a = \frac{1}{\tau_L} = \frac{C_0 \bar{\epsilon}}{2\sigma^2}, \quad (4)$$

where σ^2 is the velocity variance. These choices for a and b give the familiar form of the Langevin equation applied to homogeneous and isotropic turbulence

$$du_i = -\frac{C_0 \bar{\epsilon}}{2\sigma^2} u_i dt + (C_0 \bar{\epsilon})^{1/2} dW_i. \quad (5)$$

The first term on the right-hand side of Eq. 5 represents local correlation (with time scale τ_L), and uniquely determines the correlation time scale of u_i ; the second term corresponds to (uncorrelated) motions on the order of the Kolmogorov scale (time scale τ_η).

2.1 Application to flows with one-dimensional inhomogeneity

For inhomogeneous applications such as the atmospheric boundary layer, Eq. 5 is no longer an appropriate model for u_i for several reasons. First, mean spatial gradients cause Eq. 5 to produce non-uniform mean particle fluxes even in the absence of gradients in particle concentration. This implies that models based

143 on Eq. 5 will violate the second law of thermodynamics, considering that a
 144 nonuniform mean flux in a uniformly distributed particle plume will “un-mix”
 145 itself or decrease in entropy over time. Secondly, the presence of heterogeneity
 146 implies that $2\sigma^2/C_0\bar{\varepsilon}$ is no longer the proper correlation time scale.

147 To obtain a consistent model for u_i , we first assume a form of the (Eulerian)
 148 probability distribution of u_i . If the assumption is made that u_i is Gaussian
 149 and isotropic, the Eulerian velocity probability distribution at any instant is
 150 given by

$$P_E(\mathbf{u}; \mathbf{x}) = \frac{1}{\sqrt{2\pi}\sigma(\mathbf{x})} \exp\left(-\frac{\mathbf{u}\mathbf{u}^T}{2\sigma^2(\mathbf{x})}\right). \quad (6)$$

151 This can be substituted into the Fokker-Planck equation, along with the
 152 previous assumption that $b^2 = C_0\bar{\varepsilon}$, to yield a consistent Langevin equation
 153 for u_i (cf. Thomson, 1987; Rodean, 1996)

$$du_i = \underbrace{-\frac{C_0\bar{\varepsilon}}{2\sigma^2}u_i dt}_{\text{I}} + \underbrace{\frac{1}{2}\left(\frac{\partial\sigma^2}{\partial x_i} + \frac{u_i}{\sigma^2}\frac{d\sigma^2}{dt}\right)dt}_{\text{II}} + \underbrace{(C_0\bar{\varepsilon})^{1/2}dW_i}_{\text{III}}, \quad (7)$$

154 where $d\sigma^2/dt = \partial\sigma^2/\partial t + (U_j + u_j)(\partial\sigma^2/\partial x_j)$. The traditional interpretation
 155 of the model terms (e.g., Rodean, 1996) is that term I is the “fading memory”
 156 of the particle’s earlier velocity, term II is a “drift correction” that accounts
 157 for flow heterogeneity, and term III accounts for random pressure fluctuations
 158 with very short time scales. Determining the Langevin coefficients in this way
 159 leads to a Lagrangian dispersion model that theoretically adheres to the second
 160 law of thermodynamics, which is that an initially uniformly distributed (well-
 161 mixed) plume of particles cannot un-mix itself in the absence of sources or
 162 sinks (i.e., entropy cannot decrease).

163 2.2 Alternative interpretation of terms

164 A new grouping and interpretation of terms is proposed, which will aid in later
 165 discussion. Equation 7 can be equivalently written as

$$du_i = \underbrace{-\frac{C_0\bar{\varepsilon}}{2\sigma^2}u_i dt}_{\text{I}} + \underbrace{\frac{1}{2\sigma^2}\frac{d\sigma^2}{dt}u_i dt}_{\text{II}} + \underbrace{\frac{1}{2}\frac{\partial\sigma^2}{\partial x_i}dt}_{\text{III}} + \underbrace{(C_0\bar{\varepsilon})^{1/2}dW_i}_{\text{IV}}, \quad (8)$$

166 where term I can be interpreted as deceleration due to energy dissipation by
 167 viscosity. Since $C_0\bar{\varepsilon}/2\sigma^2$ is always positive, this term always acts to damp the
 168 particle velocity and relax it toward the mean exponentially in time. Term
 169 II is an energy production/destruction term; if the sign of $d\sigma^2/dt$ is positive
 170 (negative), correlated energy is added to (removed from) the particle velocity.
 171 Term III (along with term II) enforces the inherent requirement that the mean
 172 of the velocity fluctuations must be zero. Finally, term IV is a random forcing
 173 term corresponding to turbulent diffusion. As was the case in Eq. 5, the roles

174 of terms I and IV are to add energy (term IV) and remove energy (term I) at
 175 rates consistent with the prescribed values of σ^2 and $\bar{\varepsilon}$.

176 Heterogeneity in σ^2 causes term I to induce a mean diffusive particle flux.
 177 This is because in regions of small σ^2 , term I removes energy at a more rapid
 178 rate. As a result, particles decelerate in these regions on average, causing a
 179 build-up of particles or a convergence. To counteract this mean flux, terms
 180 II and III collectively give an ensemble mean acceleration of $\partial\sigma^2/\partial x_i$. It is
 181 clear that term III represents exactly half of this acceleration, and the average
 182 acceleration given by term II is also $\frac{1}{2}\partial\sigma^2/\partial x_i$. To see this consider a steady,
 183 one-dimensional example where $d\sigma^2/dt = u(\partial\sigma^2/\partial x)$. When the average is
 184 taken, $\overline{u^2}$ cancels with σ^{-2} to give an average acceleration of $\frac{1}{2}\partial\sigma^2/\partial x$. The
 185 other role of term II is to ensure that the ensemble u_i has the correct local vari-
 186 ance by increasing/decreasing particle energy as particles traverse a gradient
 187 in σ^2 .

188 Terms I and II represent correlated particle accelerations, whereas terms
 189 III and IV are uncorrelated. Terms I and II can be re-written in the form

$$-\frac{u_i}{\tau} = -\left(\frac{C_0\bar{\varepsilon}}{2\sigma^2} - \frac{1}{2\sigma^2} \frac{d\sigma^2}{dt}\right) u_i, \quad (9)$$

190 with the correlation time scale being

$$\tau = \left(\frac{C_0\bar{\varepsilon}}{2\sigma^2} - \frac{1}{2\sigma^2} \frac{d\sigma^2}{dt}\right)^{-1}. \quad (10)$$

191 Although this is the correlation time scale, it could equivalently be viewed as
 192 the time scale associated with energy production/dissipation. Loosely speak-
 193 ing, $C_0\bar{\varepsilon}/2\sigma^2$ can be interpreted as the *local* component of the time scale due to
 194 dissipation by viscosity, and $\frac{1}{2\sigma^2} \frac{d\sigma^2}{dt}$ the component corresponding to changes
 195 in correlation due to gradients in the velocity variance along the particle path.
 196 Note that at any instant, τ may be negative, which indicates that the particle
 197 has gained more energy due to the gradient in σ^2 than viscosity can dissipate.
 198 However, the integral time scale τ_L will always be positive for any bounded or
 199 periodic flow because any energy gained due to $d\sigma^2/dt > 0$ will be removed by
 200 a corresponding region of $d\sigma^2/dt < 0$ (or the particle could reach an indefinite
 201 region of $d\sigma^2/dt = 0$, in which case no energy is added or removed).

202 2.3 Numerical integration

203 Equation 5 can be discretized into time increments of Δt to numerically cal-
 204 culate the evolution of u_i . Using a simple explicit forward Euler scheme, this
 205 can be written for homogeneous isotropic turbulence as

$$u_i^{n+1} = u_i^n - \left(\frac{C_0\bar{\varepsilon}}{2\sigma^2}\right)^n u_i^n \Delta t + (C_0\bar{\varepsilon}^n)^{1/2} \Delta W_i, \quad (11)$$

206 where superscripts n and $n + 1$ correspond to evaluations at times of t and
 207 $t + \Delta t$, respectively. Since C_0 , $\bar{\varepsilon}$, and σ^2 are all positive (and subsequently the
 208 integral time scale is always positive), this scheme is numerically stable (in the
 209 absolute sense) when $C_0\bar{\varepsilon}\Delta t < 4\sigma^2$ (Leveque, 2007).

210 Equation 11 can be modified to include the effects of heterogeneity in σ^2
 211 to give the discrete version of Eq. 8 as

$$u_i^{n+1} = u_i^n - \left(\frac{C_0\bar{\varepsilon}}{2\sigma^2} - \frac{1}{2\sigma^2} \frac{\Delta\sigma^2}{\Delta t} \right)^n u_i^n \Delta t + \frac{1}{2} \left(\frac{\partial\sigma^2}{\partial x_i} \right)^n \Delta t + (C_0\bar{\varepsilon}^n)^{1/2} \Delta W_i. \quad (12)$$

212 where $(\Delta\sigma^2)^n$ is approximated as $(\sigma^2)^n - (\sigma^2)^{n-1}$. It should be noted that
 213 spatial derivatives have not been discretized at this point, as they are assumed
 214 to be an ‘input’ value.

215 As was previously discussed, the addition of heterogeneity results in the
 216 additional mean flux term, as well as the production/destruction term. By
 217 applying stability analysis (Leveque, 2007), it is found that Eq. 12 is unstable
 218 when the correlation time scale is negative (i.e., $C_0\bar{\varepsilon} < \Delta\sigma^2/\Delta t$), or when the
 219 correlation time scale is positive and

$$\left(C_0\bar{\varepsilon} - \frac{\Delta\sigma^2}{\Delta t} \right) \Delta t > 4\sigma^2. \quad (13)$$

220 Here, the term ‘unstable’ refers to stability in the absolute sense, which means
 221 that the truncation error grows from time t to $t + \Delta t$. As a result, the numerical
 222 error in the particle velocity does not necessarily become unsuitably large over
 223 a single timestep. But with enough consecutive timesteps where the numerical
 224 integration is ‘unstable’, the numerical error can grow to overwhelm the calcula-
 225 tion. In this case, the numerical error adds more energy than the dissipation
 226 due to viscosity plus numerical dissipation can remove, which is analogous
 227 to the above discussion in which $\tau_L < 0$. This is problematic because when
 228 a threshold value is chosen to screen for rogue trajectories, particles can be
 229 continually adding erroneous energy to the calculation without exceeding the
 230 threshold.

231 2.4 A numerically stable integration scheme

232 A common strategy for dealing with stiff differential equations is to use a nu-
 233 merical integration scheme with a large region of absolute stability (Hairer and
 234 Wanner, 1996; Leveque, 2007). Implicit schemes generally have much larger
 235 regions of absolute stability than explicit schemes such as the forward Euler
 236 scheme. In fully implicit schemes, terms are evaluated at the end of the discrete
 237 time increment rather than at the beginning. The complex nature of the prob-
 238 lem at hand means that formulating an implicit scheme is not straightforward
 239 for several reasons, each to be addressed in this section.

240 If we begin by considering the integration of Eq. 8 using a fully implicit
 241 numerical scheme, there is a problem that seemingly arises. In order to evaluate
 242 coefficients such as $\bar{\varepsilon}$, σ^2 , etc. at time $t + \Delta t$, we must not only find the unknown
 243 velocity at this time, but also the unknown particle position. This means that
 244 an iterative solution would be required for $u_i(t + \Delta t)$, which is usually quite
 245 costly. One way of dealing with this is to ‘lag’ the coefficients, which means
 246 evaluating the coefficients at time t but evaluating the velocity at $t + \Delta t$. This
 247 may result in a slight loss of accuracy, but this loss is usually found not to
 248 be significant (Leveque, 2007). If the coefficients are lagged, Eq. 8 can now be
 249 written using a fully implicit scheme (backward Euler) as

$$u_i^{n+1} = u_i^n - \left(\frac{C_0 \bar{\varepsilon}}{2\sigma^2} - \frac{1}{2\sigma^2} \frac{\Delta\sigma^2}{\Delta t} \right)^n u_i^{n+1} \Delta t + \frac{1}{2} \left(\frac{\partial\sigma^2}{\partial x_i} \right)^n \Delta t + (C_0 \bar{\varepsilon}^n)^{1/2} \Delta W_i, \quad (14)$$

250 where $(\Delta\sigma^2)^n$ is approximated as $(\sigma^2)^n - (\sigma^2)^{n-1}$. Note that all coefficients
 251 are evaluated at time n , and that u_i is evaluated at time $n + 1$. It is then
 252 straightforward to obtain an algebraic solution for u_i^{n+1} .

253 The scheme is stable for all $\tau_L > 0$. As was discussed in the previous
 254 section, τ_L will never be negative due to the particle dynamics alone, and
 255 the use of an implicit scheme means that numerical error will also not make
 256 τ_L negative. Therefore, the implicit scheme should be unconditionally stable
 257 (which will be demonstrated in the following sections).

258 One important additional item to note about Eq. 14 is that the total deriva-
 259 tive of σ^2 is discretized directly as $(\Delta\sigma^2/\Delta t)^n = [(\sigma^2)^n - (\sigma^2)^{n-1}]/\Delta t$ rather
 260 than $(\partial\sigma^2/\partial t)^n + u_j^{n+1} (\partial\sigma^2/\partial x_j)^n$. In other words, the total derivative is cal-
 261 culated along particle trajectories (Lagrangian) rather than using the Eulerian
 262 definition at a fixed grid point. Using the Eulerian approach would make Eq. 14
 263 non-linear in u_i^{n+1} , thus eliminating the possibility for an explicit algebraic so-
 264 lution for u_i^{n+1} . For consistency, the same Lagrangian approach was used for
 265 the explicit method (Eq. 12), although the Eulerian approach was also tested
 266 to ensure that it did not significantly change results.

267 2.4.1 Generalization to three-dimensional, heterogeneous, anisotropic 268 turbulence

269 This analysis can be easily generalized to cases of anisotropic turbulence. We
 270 can proceed by assuming a form for the Eulerian velocity probability distri-
 271 bution function in terms of the macroscopic velocity covariances

$$P_E = (2\pi)^{-3/2} (\det \mathbf{R})^{-1/2} \exp\left(-\frac{1}{2} \mathbf{u}^T \mathbf{R}^{-1} \mathbf{u}\right), \quad (15)$$

272 where $\mathbf{R} = R_{ij}$ is the Reynolds stress (or velocity covariance) tensor, \mathbf{R}^{-1} is
 273 its inverse, and \mathbf{u}^T is the transpose of \mathbf{u} . It is clear that \mathbf{R} must be positive
 274 semi-definite, otherwise the argument to the exponential function is positive

275 and $P_E \rightarrow \infty$ as $|\mathbf{u}| \rightarrow \infty$. It is known that a true Reynolds stress tensor is
 276 positive semi-definite by definition (Du Vachat, 1977; Schumann, 1977), but
 277 modelled stress tensors may not necessarily satisfy this condition. \mathbf{R} must also
 278 be non-singular since this formulation for P_E involves a division by $\det \mathbf{R}$.
 279 When such conditions are satisfied, the tensor is termed ‘realizable’. A new
 280 method for ensuring realizability is suggested in Sect. 5.3 for cases where the
 281 modelled Reynolds stress tensor is not necessarily realizable because it is not
 282 a true covariance tensor.

283 Thomson (1987) substituted Eq. 15 along with the previous expression for
 284 b into the Fokker-Planck equation to solve for the coefficient a . Although the
 285 solution is not unique, Thomson’s ‘simplest’ model for dispersion in Gaussian,
 286 inhomogeneous, and anisotropic turbulence was given as

$$du_i = -\frac{C_0 \bar{\varepsilon}}{2} R_{ik}^{-1} u_k dt + \frac{R_{\ell j}^{-1}}{2} \frac{dR_{i\ell}}{dt} u_j dt + \frac{1}{2} \frac{\partial R_{i\ell}}{\partial x_\ell} dt + (C_0 \bar{\varepsilon})^{1/2} dW_i. \quad (16)$$

287 We can obtain an implicit scheme in a manner analogous to the isotropic
 288 turbulence case

$$u_i^{n+1} = u_i^n - \left(\frac{C_0 \bar{\varepsilon}}{2} R_{ik}^{-1} \right)^n u_k^{n+1} \Delta t + \left(\frac{R_{\ell j}^{-1}}{2} \frac{\Delta R_{i\ell}}{\Delta t} \right)^n u_j^{n+1} \Delta t + \frac{1}{2} \left(\frac{\partial R_{i\ell}}{\partial x_\ell} \right)^n \Delta t + (C_0 \bar{\varepsilon}^n)^{1/2} \Delta W_i, \quad (17)$$

289 where $(\Delta R_{i\ell})^n = [(R_{i\ell})^n - (R_{i\ell})^{n-1}]$. The resulting scheme is unconditionally
 290 stable provided that R_{ij} is realizable.

291 Equation 17 is a 3×3 matrix system of equations in terms of u_i , which can
 292 be easily inverted analytically. Clearly the system of equations given by Eq. 17
 293 must be non-singular to allow for inversion. However, since velocity increments
 294 are generally small compared to the velocity itself, the author has never found
 295 any instances where singularity was a problem, as the determinant is generally
 296 of order unity.

297 2.5 Some notes on increasing numerical accuracy

298 If higher numerical accuracy is desired, one could use a numerical integration
 299 scheme with a higher order of accuracy. Higher-order schemes are available
 300 (Kloeden and Platen, 1992), but we are limited by the fact that we either
 301 have to lag the coefficients, or else we end up with a costly iterative solution.

302 Although many approaches are available to increase numerical accuracy,
 303 the present work controls the accuracy by varying Δt ; Δt could be adjusted
 304 autonomously using a standard adaptive timestepping approach (Press et al,
 305 2007), although not explored here. These methods generally proceed as follows:

306 a step of size Δt^n is taken at some time t and the error of the step is estimated.
 307 If that error is less than some predefined tolerance, the timestep is increased for
 308 the next iteration in time. If the estimated error is greater than the tolerance,
 309 the step is rejected and re-tried with a smaller step size until the error is
 310 below the tolerance. There are some complications that arise when dealing
 311 with stochastic differential equations, which are described in, e.g., Mauthner
 312 (1998) and Lamba (2003).

313 3 Sinusoidal test case

314 3.1 Test case set-up

315 To analyze the performance of the proposed methodology in Reynolds-averaged
 316 applications, a simple isotropic turbulence field was formulated to facilitate
 317 straightforward analysis. The required Eulerian statistics of the velocity field
 318 were specified as

$$\sigma^2(x) = 1.1 + \sin x, \quad (18a)$$

$$\bar{\varepsilon}(x) = \sigma^3(x), \quad (18b)$$

319 such that $0 \leq x \leq L$, where here $L = 2\pi$. A graphical depiction of σ^2 and $\bar{\varepsilon}$
 320 is given in Fig. 1. The equation for $\bar{\varepsilon}$ stems from the scaling argument that
 321 $\varepsilon \sim k^{3/2}/\ell$ and $k \sim \sigma^2$, where k is the turbulent kinetic energy and ℓ is a
 322 characteristic length scale for energetic eddies. However the choices for σ^2 and
 323 $\bar{\varepsilon}$ are arbitrary, as these are model inputs. The goal of the model is to produce
 324 particle velocities whose statistics are consistent with the specified inputs,
 325 whether they be physical or non-physical. A sinusoid was chosen because it
 326 is periodic, and has regular intervals of heterogeneity; furthermore, it means
 327 that function evaluations and derivatives are exact. All units in this section
 328 are arbitrary; each component of the mean velocity U_i was set to zero for these
 329 tests.

330 In the test simulations, 100,000 particles were released from random points
 331 uniformly distributed over the interval $(0, 2\pi)$. Particle trajectories followed a
 332 periodic condition at the flow boundaries $x/L = 0$ and 1; they were tracked
 333 over a time period of $T = 10$. C_0 was taken to be equal to 4.0, and unless
 334 otherwise noted $\Delta t = 0.1$. The particle velocity was initialized by drawing a
 335 Gaussian random number with mean zero and variance $\sigma^2(x_0)$, where x_0 is
 336 the particle's initial position.

337 The ‘mixedness’ of the particle plume was quantified using the entropy ‘ S ’,
 338 which, following the common approach used in information theory, is defined
 339 as

$$S = - \sum_{i=1}^{N_{bins}} P(x_i) \ln P(x_i), \quad (19)$$

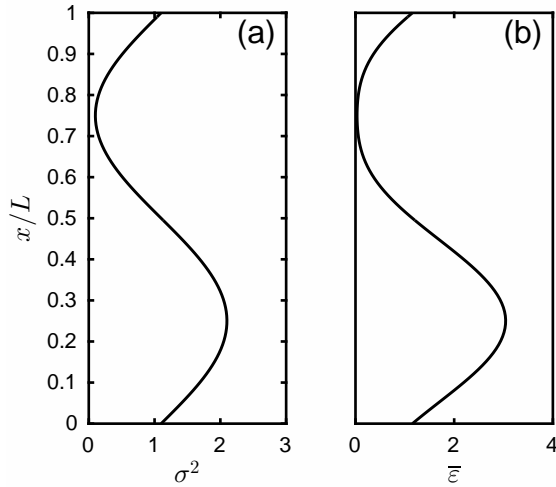


Fig. 1 Profiles of turbulence quantities in the sinusoidal test case: (a) velocity variance σ^2 , and (b) average turbulence dissipation rate $\bar{\epsilon}$.

340 where $P(x_i)$ is the probability that a particle resides in the i^{th} discrete subin-
 341 terval of x ($i = 1, 2, \dots, N_{bins}$). When calculated in this way, the entropy of the
 342 perfectly mixed particle distribution is $S = 0$. The entropy of the simulated
 343 particle plume is expected to be negative, but the goal is to achieve an entropy
 344 as close to zero as possible.

345 If a particle became ‘rogue’, it was discarded and not included in the anal-
 346 ysis. For practical purposes, a particle is considered rogue when the absolute
 347 value of its velocity exceeds $10 \max(\sigma)$. Previous work commonly uses a weaker
 348 threshold of closer to 6σ (e.g., [Wilson, 2013](#); [Postma, 2015](#)). Given the number
 349 of particle trajectory updates and the assumed velocity distribution, it is not
 350 impossible to find a stable particle with a velocity near $6 \max(\sigma)$. The odds
 351 are around 1 in 5×10^8 , and the simulations that follow have up to 10^9 particle
 352 updates. However, it would be exceedingly unlikely to find a stable particle
 353 with a velocity greater than $10 \max(\sigma)$. Experience has shown that if a particle
 354 is unstable, its velocity quickly exceeds $10 \max(\sigma)$ or even $100 \max(\sigma)$, which
 355 clearly distinguishes it from a stable particle whose velocity has become large
 356 simply because it lies in the tails of the probability distribution. Thus, it is
 357 preferable to choose a large threshold to define rogue trajectories. With this
 358 type of thresholding methodology, the cumulative number of rogue trajectories
 359 over an entire simulation is also expected to increase with the length of the
 360 simulated time period.

3.2 Particle position probability density functions

Figure 2a gives the probability density function (p.d.f.) of particle position at the end of the simulation, with u calculated according to Eq. 11 (which assumes homogeneity). For comparison, the ‘well-mixed’ particle distribution is shown by the vertical dashed line. The figure illustrates the well-known result that this methodology violates the second law of thermodynamics, and causes particles to accumulate in regions of low velocity variance (see Fig. 1). Using the known region of stability introduced earlier $\Delta t < \min(4\sigma^2/C_0\bar{\epsilon})$, the timestep should be less than about 0.7 to ensure stability. Thus, as shown in the figure, $\Delta t = 0.1$ gives no rogue trajectories. Although not shown, it was verified that at around $\Delta t \approx 0.7$, rogue trajectories began appearing as expected.

Using the inhomogeneous model for u with an explicit forward Euler integration scheme (Eq. 12) actually degraded results (Fig 2b). Firstly, the entropy substantially decreases over that of the homogeneous model; secondly, 55% of particles became rogue according to the definition given above. Note that this value of 55% increases continually in time until eventually all particles become rogue. Whether there are only a few rogue trajectories or whether there are thousands, the solution is still unstable over some region and all particles are likely to eventually become rogue if the simulation runs for long enough time.

If the same inhomogeneous model for u is used but instead with an implicit backward Euler integration scheme (Eq. 14), an improvement in results can be observed (Fig 2c). The entropy increases slightly over the homogeneous model (i.e., entropy is closer to zero), and there are no rogue trajectories as expected.

3.3 Effect of the timestep on stability and ‘mixedness’

Figure 3 shows the effect of varying the timestep for the ‘sinusoidal’ test case using the explicit inhomogeneous model for u (Eq. 12, Fig. 3a-d) and the implicit inhomogeneous model (Eq. 14, Fig. 3e-h). It should be noted that for the homogeneous model (Eq. 11), reducing the chosen timestep had little effect, and therefore no further results are shown for that case.

As the timestep is decreased when using the explicit forward Euler scheme, the frequency of rogue trajectories decreases towards zero. This is an expected result, since decreasing the timestep means that the scheme will tend toward its region of absolute stability.

It is difficult to use Eq. 13 to calculate the required timestep for stability since $\Delta\sigma^2$, or equivalently $u(\partial\sigma^2/\partial x)\Delta t$, is not readily calculated. If we estimate that $\max|u| \sim 6\max(\sigma)$, we can estimate that the explicit scheme is stable when

$$\Delta t \lesssim \min \left(\frac{4\sigma^2}{C_0\bar{\epsilon} \pm 6\max(\sigma) \frac{\partial\sigma^2}{\partial x}} \right). \quad (20)$$

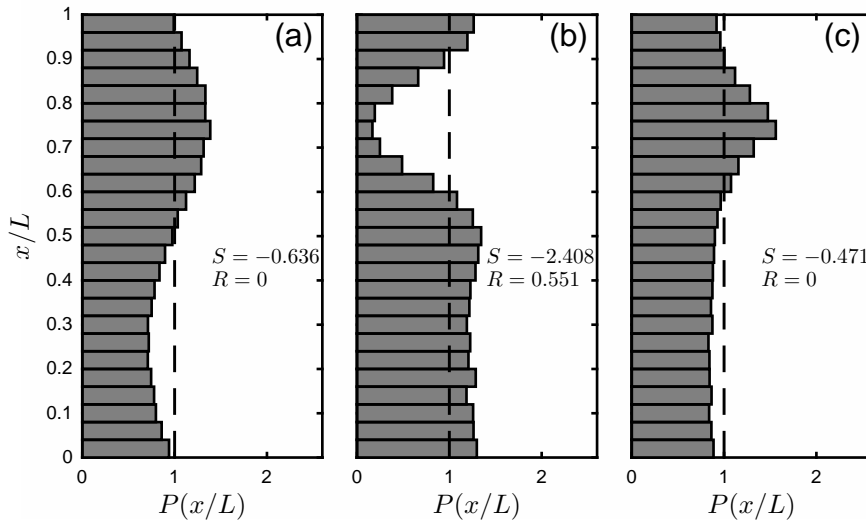


Fig. 2 P.d.f. of particle position for the sinusoidal test case: (a) homogeneous model for u (Eq. 11) integrated using an explicit forward Euler scheme ($\Delta t = 0.1$); (b) inhomogeneous model for u (Eq. 12) integrated using an explicit forward Euler scheme ($\Delta t = 0.1$); (c) inhomogeneous model for u (Eq. 14) integrated using an implicit backward Euler scheme ($\Delta t = 0.1$). R is the fraction of particles that were ‘rogue’, or $|u| > 10 \max(\sigma)$, and S is the entropy of the plume.

399 Substituting values gives that the forward Euler scheme is stable for this test
 400 case when $\Delta t \lesssim 0.03$, which agrees with Fig. 3. Note that this is only a rough
 401 estimate, and should not be considered exact. This equation can also be used
 402 to estimate the region(s) of the flow where particles are most likely to become
 403 unstable. Figure 4 shows the distribution of the locations of rogue trajectories
 404 (i.e., the particle’s location when its velocity first exceeded the threshold of
 405 $10 \max(\sigma)$), as well as the region of absolute instability as estimated from
 406 Eq. 20. Not surprisingly, rogue trajectories were most likely to occur in the
 407 region where the model equations were unstable.

408 For both the explicit and implicit integration schemes, the entropy or
 409 ‘mixedness’ tends toward zero as the timestep is decreased. However, it ap-
 410 pears that the implicit scheme approaches a well-mixed state more rapidly
 411 than the explicit scheme. For moderately small timesteps (e.g., $\Delta t = 0.1$ and
 412 0.05), the entropy is substantially lower when an implicit scheme is used. This
 413 result is important for cases where an extremely small timestep cannot be used
 414 and compromises must be made. In such cases, it appears preferable to use an
 415 implicit scheme, as it results in unconditional stability and better adherence
 416 to the well-mixed condition.

417 When the timestep was increased to extreme levels, there also became a
 418 point where the plume started tending back toward a well-mixed state. When
 419 this occurred, velocity increments were very large, and an additional diffusive
 420 effect became present, which mixed out the particle plume (see Fig. 3a,e).

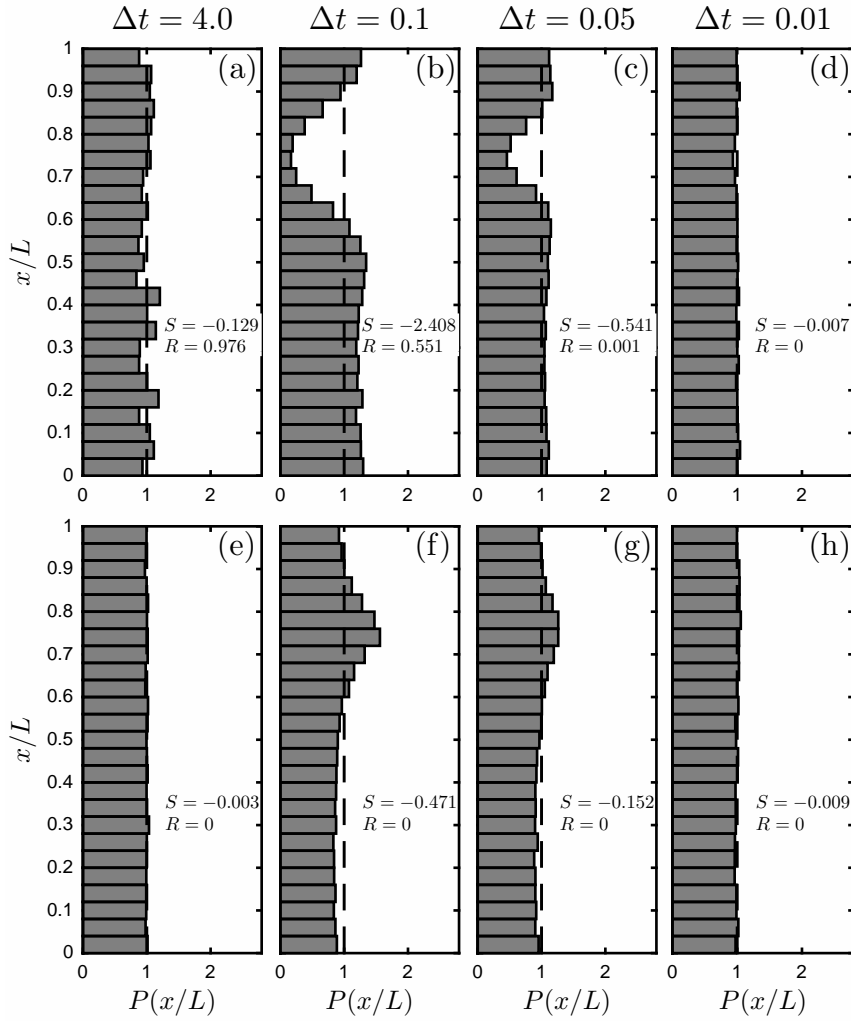


Fig. 3 P.d.f. of particle position for the sinusoidal test case using the inhomogeneous model for u (Eq. 8). Columns correspond to varying timestep. Rows correspond to varying integration scheme, with panes (a)-(d) using the explicit forward Euler scheme (Eq. 12), and panes (e)-(h) using the implicit backward Euler scheme (Eq. 14). R is the fraction of particles that were ‘rogue’, or $|u| > 10 \max(\sigma)$, and S is the entropy of the plume.

421 This happens when the particle timestep is on the order of the integral time
 422 scale. As will be further illustrated in Sect. 3.4, the WMC is seemingly satisfied
 423 because particle timesteps are so large that the particle’s variance is uncoupled
 424 with the local Eulerian variance, and thus the local gradient in the variance
 425 does not act to un-mix particles. This is an important result, as it indicates
 426 that the WMC alone is not a sufficient indicator of the performance of the
 427 numerical scheme. The next section presents a more thorough examination.

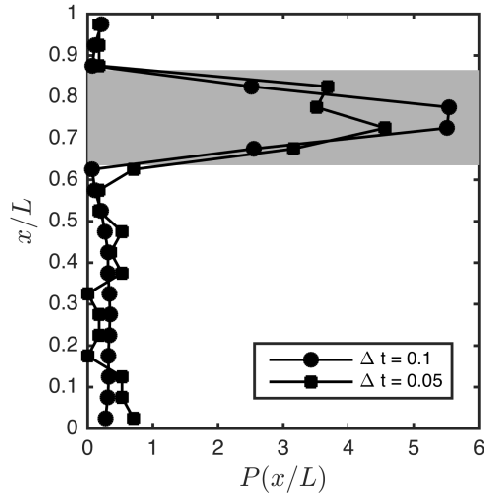


Fig. 4 Probability distribution $P(x/L)$ of the location where particles became ‘rogue’, or first exceeded the velocity threshold of $10\sigma(x)$ for two timestep choices. The shaded area shows the region of instability for $\Delta t = 0.05$, as approximated by Eq. 20.

428 3.4 Eulerian profiles of particle velocity

429 The direct purpose of the above models is not necessarily to satisfy the well-
 430 mixed condition or second law of thermodynamics (i.e., this is not the govern-
 431 ing equation being solved). Satisfying these consistency conditions is simply
 432 a byproduct. Rather, the purpose is to produce an ensemble of Lagrangian
 433 particles that has the velocity p.d.f. prescribed by Eq. 6, i.e., Gaussian with
 434 zero mean and local variance $\sigma^2(x_i)$. It will be shown that if the computed
 435 Eulerian particle velocity p.d.f. has zero mean and local variance $\sigma^2(x)$, the
 436 well-mixed condition will be satisfied by default.

437 To better assess the numerical procedure, it is instructive to calculate Eu-
 438 lerian statistics of the Lagrangian particle velocities, and compare them with
 439 the ‘exact’ values. Fortunately, the exact values of the Eulerian mean velocity
 440 and variance are always known, since they were specified as inputs. The en-
 441 semble mean particle velocity should be zero at every point, and the ensemble
 442 mean of the particle velocity increments should be equal to $\partial\sigma^2(x)/\partial x$. The
 443 ensemble particle velocity variance should be equal to $\sigma^2(x)$, and the variance
 444 of the particle velocity increments should be equal to $C_0\bar{\varepsilon}(x)\Delta t$.

445 Figures 5 and 6 compare calculated Eulerian profiles of mean particle veloc-
 446 ity, mean particle velocity increments, particle velocity variance, and variance
 447 of the particle velocity increments. These profiles are determined by estab-
 448 lishing a set of discrete spatial bins, and calculating the mean/variance of all
 449 particles residing in a given bin. This Eulerian averaging operator is denoted
 450 as $\langle \cdot \rangle_E$.

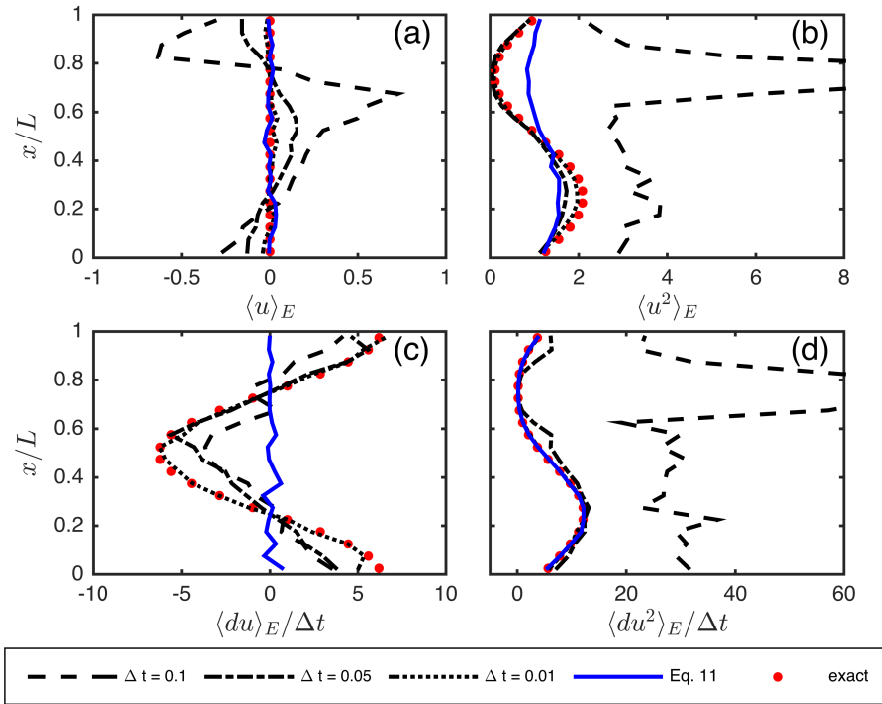


Fig. 5 Simulated Eulerian profiles for the sinusoidal test case using the explicit scheme: (a) average particle velocity, (b) particle velocity variance, (c) average particle acceleration, (d) variance of particle velocity increments. Profiles are formed by calculating an average or variance over all particles residing in the i^{th} discrete spatial bin. The *solid blue line* denotes results when the homogeneous model (Eq. 11) was used with $\Delta t = 0.01$. Note that $\Delta t = 4.0$ is not shown because so many particles were rogue that it made it difficult to obtain meaningful profiles.

451 *Homogeneous model:* When the model lacks correction terms for hetero-
 452 geneity (Eq. 11), the mean particle velocity correctly remains zero everywhere
 453 (Fig. 5a), but the particles do not assume the correct velocity variance
 454 profile (Fig. 5b). This is because the mean acceleration required for the particles
 455 to assume the correct velocity variance is not properly applied (Fig. 5c). In
 456 other words, a mean acceleration is required for particles to assume a het-
 457 erogeneous $\sigma^2(x)$ profile. Since Eq. 11 has zero mean acceleration, un-mixing
 458 occurs regardless of the timestep when σ^2 is heterogeneous (Fig. 2a).

459 *Inhomogeneous model, implicit scheme:* When the effects of instability are
 460 removed from the inhomogeneous model by using an implicit scheme, numeri-
 461 cal accuracy dictates the degree to which un-mixing occurs. Numerical errors
 462 lead to particle ensembles that deviate from the ‘exact’ Eulerian statistics
 463 specified as inputs (Fig. 6). Errors induce a non-zero Eulerian mean particle
 464 velocity (Fig. 6a), and cause particles to fail to assume the correct variance

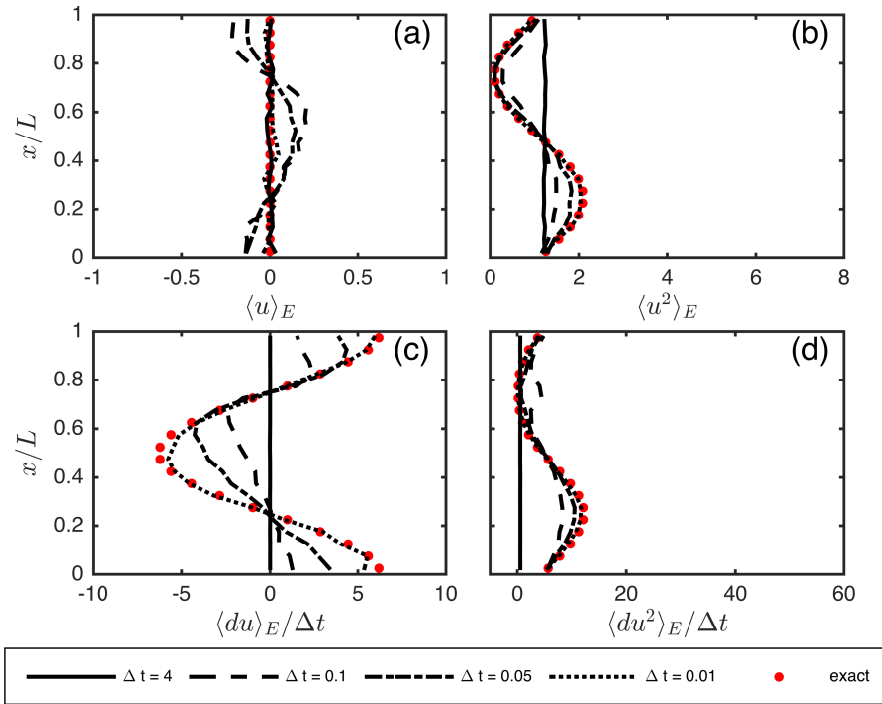


Fig. 6 Same as Fig. 5 except that the implicit integration scheme was used.

465 distribution (Fig. 6b). When the timestep is too large, the model fails to correctly
 466 represent the mean acceleration that corrects for the effects of heterogeneity
 467 (Fig. 6c) and the variance of the velocity increments (Fig. 6d). When
 468 the timestep is extremely large, the model correctly predicts a zero ensemble
 469 mean particle velocity everywhere, but an incorrect velocity variance profile
 470 that is uniform. The uniform variance profile explains why no un-mixing is
 471 observed in Fig. 3e.

472 The mean velocity induced by numerical errors (Fig. 6a) appears to be
 473 consistent with the un-mixing patterns shown in Fig. 3e-h. The change in sign
 474 of in $\langle u \rangle_E$ at $x/L \approx 0.75$ causes a convergence, while the change in sign at
 475 $x/L \approx 0.25$ causes a divergence. However, it can be seen from Fig. 3e-h that the
 476 convergence at $x/L \approx 0.75$ is much larger than the divergence at $x/L \approx 0.25$.
 477 This is due to the fact that the velocity variance (or standard deviation) is
 478 much smaller at $x/L \approx 0.75$, and thus the induced mean velocity has a much
 479 larger effect (i.e., $\langle u \rangle_E / \sigma$ is much larger at $x/L \approx 0.75$).

480 *Inhomogeneous model, explicit scheme:* The explicit scheme showed similar
 481 behaviour in the induced mean velocity and acceleration profiles as the
 482 timestep was varied (Fig. 6a,c). The primary difference when compared with
 483 the implicit scheme was that when the timestep was moderately large, the

484 explicit scheme added too much energy (Fig. 6b,d). An exceptionally large
 485 spike in particle energy can be found near $x/L \approx 0.75$, which corresponds
 486 to the most probable location of instability (Fig. 4). Thus, it appears that
 487 instabilities act to add erroneous energy to the particles.

488 Interestingly, the patterns in un-mixing for the explicit scheme (Fig. 3a-
 489 d) are opposite of the implicit scheme, where a strong divergence is found at
 490 $x/L \approx 0.75$ rather than a convergence. It is probable that this is related to the
 491 presence of instabilities. As was previously shown, instabilities add erroneous
 492 energy, which is strongest at $x/L \approx 0.75$. This energy is liable to create a
 493 diffusive effect that will cause particles to vacate this region, thus resulting in
 494 a divergence. However, it is difficult to demonstrate directly that this is the
 495 case, as the effects of instability and numerical inaccuracy cannot be readily
 496 separated for the explicit scheme.

497 3.5 Effect of numerical interpolation and differentiation

498 In the above methodology, coefficient evaluations and spatial derivatives were
 499 exact since explicit equations were available for σ^2 and $\bar{\epsilon}$. However, in most
 500 real situations, only discrete ‘gridded’ data are available. This means that in
 501 order to evaluate, e.g., $\sigma^2(x_i)$, a numerical interpolation scheme must be used.
 502 Additionally, spatial derivatives such as $\partial\sigma^2/\partial x_i$ must be estimated using a
 503 numerical scheme. Since the above section found that numerical accuracy in
 504 integrating the differential equation for u_i affected the degree to which the
 505 well-mixed condition was satisfied, it is reasonable to imagine that numerical
 506 accuracy of the interpolation and spatial differentiation schemes may also play
 507 a role.

508 The previous simulations were repeated using a discrete grid of 20 points,
 509 with linear interpolation used for function evaluations between discrete points.
 510 Spatial derivatives were calculated at each grid point using a centred finite
 511 difference scheme, which were interpolated between grid points using a linear
 512 scheme (both of which are second-order accurate). When this approach was
 513 used, no significant differences were found in Figs. 2 or 3. It was found that as
 514 long as the Eulerian grid was fine enough to adequately resolve mean spatial
 515 gradients, numerical errors in the differencing and interpolation schemes had
 516 a minimal overall effect on the ability of model outputs to match the specified
 517 input fields. In the following section, cases are noted where very large gradients
 518 in $\sigma^2(x)$ caused difficulty in the numerical estimation of gradients, and some
 519 simple solutions are suggested.

520 4 Channel flow test case

521 4.1 Test case set-up

522 The simplicity of the above sinusoidal test case provided a convenient means for
 523 testing the given numerical schemes. However, such a case is clearly unphysical.

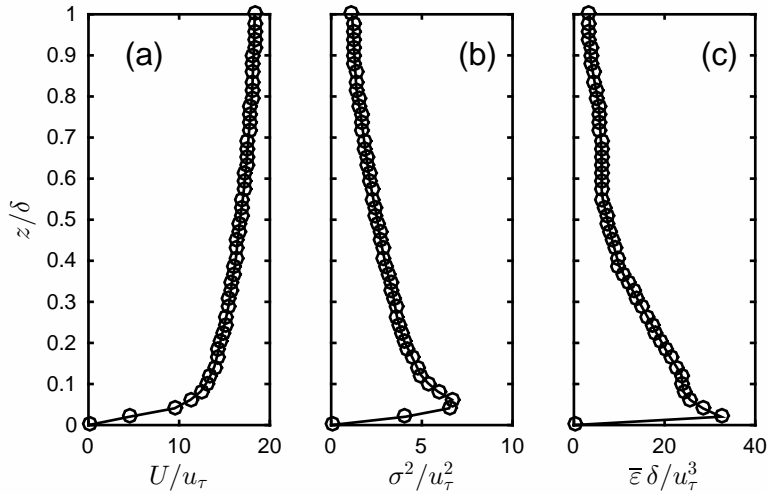


Fig. 7 Input profiles for channel flow test case: (a) mean velocity magnitude, (b) isotropic velocity variance, and (c) mean turbulence dissipation rate. Profiles are normalized using the friction velocity scale u_τ and the channel half-height δ .

524 To demonstrate that the above analysis still holds in a more realistic case, a
 525 channel flow was considered. The channel flow direct numerical simulation
 526 (DNS) data of Kim et al (1987) and Mansour et al (1988) were used to drive
 527 the dispersion simulations. Horizontally-averaged profiles were calculated from
 528 the DNS data set in order to set up a one-dimensionally inhomogeneous flow
 529 that could be used to test the Reynolds-averaged models. In this section, only
 530 the isotropic model is considered, with testing of the anisotropic model left for
 531 the next section.

532 Profiles of the normalized mean velocity U , the velocity variance σ^2 , and
 533 turbulence dissipation rate $\bar{\epsilon}$ are given in Fig. 7, whose values were defined on
 534 50 uniform grid points. Dimensional values are normalized by some combina-
 535 tion of the channel half-height δ and the friction velocity u_τ . The simulations
 536 were set up such that particle position and velocity evolved through time in
 537 all three Cartesian coordinate directions, although only transport in the wall-
 538 normal direction will be examined. The mean velocity was equal to U in the
 539 streamwise (x) direction, and zero in other directions. The Eulerian velocity
 540 variance was equal to σ^2 in all three Cartesian directions (isotropic). Note
 541 that the isotropic velocity variance was specified as $\sigma^2 = \frac{2}{3}k$, where k is the
 542 turbulent kinetic energy.

543 100,000 particles were uniformly released at $t = 0$, and simulated for a
 544 period of $T = \delta u_\tau^{-1}$. C_0 was set equal to 4.0.

545 4.1.1 Boundaries

546 The zero-flux boundaries raised some questions in the model. The first is how
547 the boundaries should impact particle motion. Because the particles are simply
548 fluid parcels with no mass, in reality such particles generally never impact the
549 wall. As real particles approach the wall, their velocity is damped to zero by
550 viscosity before impacting the wall. Thus particle velocities should approach
551 zero at the lower wall, and the vertical velocity component should approach
552 zero at the upper boundary. The models used in this work do not have a
553 viscous sublayer model, and therefore particles do not necessarily obey such
554 constraints. The strategy used in this work was to enforce that all variables go
555 to zero at the lowest grid point, and all gradients and vertical fluxes go to zero
556 at the highest grid point. In this case, particles tended to naturally follow the
557 zero-flux wall boundary conditions on their own. Cases where particles still
558 crossed boundaries were due to numerical inaccuracies, and in general as the
559 numerical solution converged, fewer and fewer wall crossings were observed. To
560 ensure the boundary conditions were always enforced regardless of numerical
561 errors, perfect reflection was used.

562 Another boundary-related issue was with regard to calculation of vertical
563 gradients. When gradients were numerically calculated in the previous test
564 case, a central differencing scheme was used throughout, which was made possible
565 by the fact that boundaries were periodic. Near zero-flux boundaries, a
566 forward (backward) scheme must be used at the lower (upper) boundaries.
567 Switching schemes near the walls tended to create problems related to the
568 model's ability to satisfy the well-mixed condition in those areas. This caused
569 un-mixing to occur near the boundaries regardless of how small of a timestep
570 was used. Two possible remedies were found that prevented this from hap-
571 pening. One was to linearly interpolate gridded data onto a finer grid such
572 that near-boundary gradients were well-resolved. Another was to use the same
573 scheme throughout the domain as is used at the lower wall (i.e., a forward
574 scheme). This still requires a change in schemes at the upper wall, but if gra-
575 dients are small there, it did not seem to create a problem. In what follows,
576 a second-order forward differencing scheme was used for all nodes except at
577 the top two nodes, in which case a second-order backward scheme was used.
578 Furthermore, 50 vertical grid points were chosen so that there was at least one
579 grid point between the lower wall and the point where σ^2 begins to rapidly
580 decrease.

581 4.2 Particle position p.d.f.s

582 First, the model's ability to satisfy the WMC or thermodynamic constraint
583 was assessed. Figure 8 gives the probability distribution of vertical particle
584 position at the end of the simulation. Results showed similar behaviour as in
585 the previous 'sinusoidal' test case. Using the forward Euler scheme resulted in
586 a substantial number of rogue trajectories, which decreased as the timestep

587 was decreased. The frequency of rogue trajectories was seemingly less than for
 588 the sinusoidal case, but this could likely be related to simulation duration. If
 589 the simulation were to run for longer, rogue trajectories would increasingly
 590 accumulate.

591 For moderately small timesteps ($\Delta t = 0.01 \delta u_{\tau}^{-1}$), the backward Euler
 592 scheme gave a more well-mixed plume than the forward Euler scheme, in
 593 addition to ensuring stability. For very small timesteps ($\Delta t = 10^{-4} \delta u_{\tau}^{-1}$),
 594 both schemes gave a very well-mixed plume and zero rogue trajectories. Using
 595 Eq. 20, it was estimated that a timestep of $\Delta t \lesssim 0.004 \delta u_{\tau}^{-1}$ was required for
 596 stability. The simulations were used to confirm that rogue trajectories started
 597 appearing at roughly $\Delta t > 10^{-3} \delta u_{\tau}^{-1}$. It is notable that if a small amount of
 598 un-mixing is tolerable, the implicit scheme allowed Δt to be increased by one
 599 or even two orders of magnitude while still achieving stability.

600 4.3 Eulerian profiles of particle velocity

601 Figures 9 and 10 depict the ability of the models to match Eulerian statis-
 602 tics given as inputs for several different timestep choices. As expected, refin-
 603 ing the timestep leads to a convergence of the solution toward the specified
 604 Eulerian statistics. Using too large of a timestep induces a mean vertical ve-
 605 locity that tends to un-mix particle plumes. Instabilities resulting from the
 606 forward Euler integration scheme tended to add far too much energy to the
 607 particles, resulting in over prediction of the variance of the vertical velocity
 608 and velocity increments. In general, numerical errors in the implicit backward
 609 Euler scheme tended to under predict variances. For intermediate timesteps
 610 (e.g., $\Delta t = 0.01 \delta u_{\tau}^{-1}$), the implicit scheme was much better than the explicit
 611 scheme at predicting Eulerian profiles, which is likely due to errors associated
 612 with instabilities when the explicit scheme was used.

613 5 Large-eddy simulation and anisotropic models

614 5.1 Model formulation

615 All of the above analysis was performed in the context of modeling the fluctu-
 616 ating velocity resulting from Reynolds decomposition. A natural generalization
 617 can be made to extend the analysis to large-eddy simulation (LES) models.
 618 This analysis is also relevant to readers only interested in Reynolds-averaged
 619 models, as the close similarities of the LES and Reynolds-averaged formula-
 620 tions means that the LES models can be used to illustrate the feasibility of
 621 the methods in any general anisotropic flow scenarios.

622 In LES, turbulent length scales larger than the numerical grid scale Δ are
 623 calculated directly from the filtered Navier-Stokes equations, while smaller

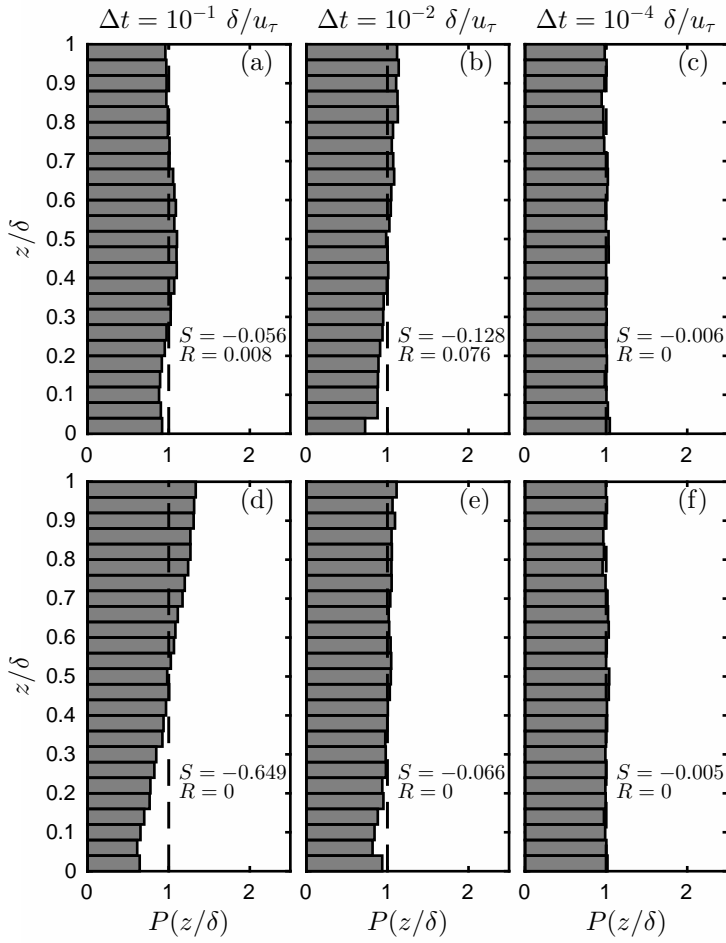


Fig. 8 Probability density functions of particle position for the channel flow test case using the inhomogeneous model for u_i (Eq. 8). Columns correspond to varying timestep (values given at the top of columns). Rows correspond to varying integration scheme, with panes (a)-(c) using the explicit forward Euler scheme (Eq. 12), and panes (d)-(f) using the implicit backward Euler scheme (Eq. 14). R is the fraction of particles that were ‘rogue’, or $|u_i| > 10 \max(\sigma)$.

624 scales are modelled. Using this approach, the evolution of a particle’s position
 625 with time can be written as

$$\frac{dx_{p,i}}{dt} = \tilde{u}_i + u_{s,i}, \quad (21)$$

626 where \tilde{u}_i is the resolved particle velocity, which is available from the LES solu-
 627 tion assuming the particle velocity is equal to the Eulerian fluid velocity at the
 628 point $x_{p,i}$. $u_{s,i}$ is the unresolved (subfilter-scale) particle velocity, which must
 629 be modelled. This approach has a considerable advantage over the traditional

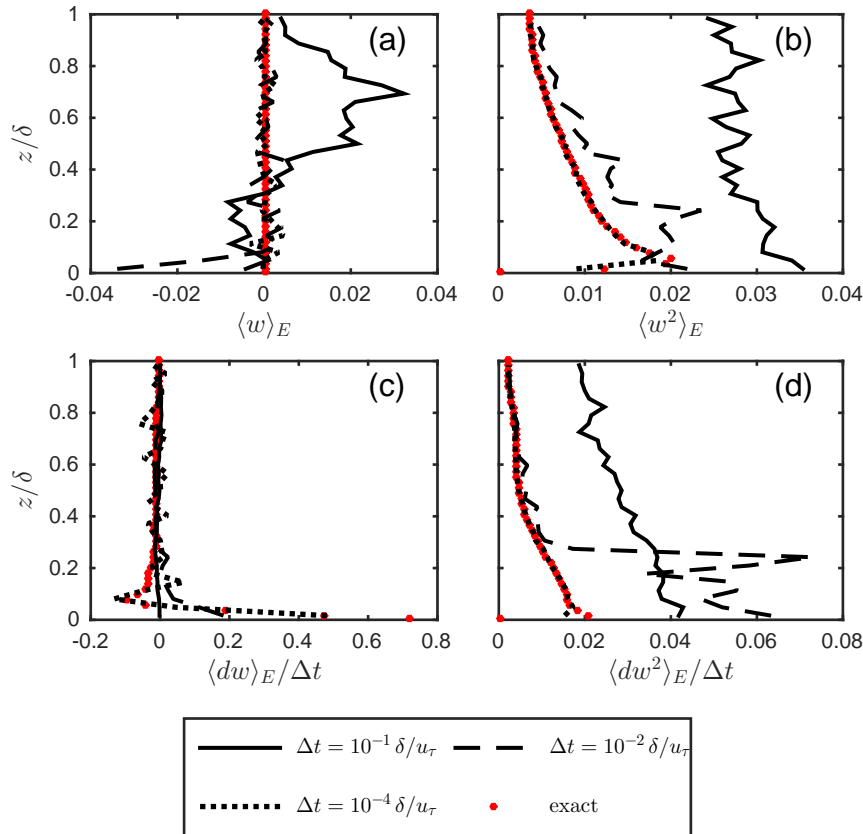


Fig. 9 Eulerian particle velocity statistics for the channel flow test case when an explicit forward Euler integration scheme was used. Calculated profiles are compared to exact profiles for (a) average particle vertical velocity, (b) particle vertical velocity variance, (c) average vertical particle acceleration, (d) variance of particle vertical velocity increments. Profiles are formed by calculating an average or variance over all particles residing in the i^{th} discrete spatial bin.

630 Reynolds-averaged approach described in Sect. 2 in that $u_{s,i}$ presumably contains
 631 only the small ‘universal’ scales of motion, which are more likely to follow
 632 standard gradient-diffusion theory.

633 LES Lagrangian dispersion models have generally paralleled Reynolds-
 634 averaged models. The underlying theme in essentially all LES models is they
 635 assume that models for the velocity fluctuations from the ensemble mean can
 636 be applied to fluctuations from the filtered velocity (with a few minor modifica-
 637 tions). In theory, this assumption seems reasonable as the ensemble averaging
 638 operator is simply a filter over all scales.

639 It is assumed that the subfilter-scale velocity has a Gaussian distribution of
 640 a form analogous to Eq. 15, but with the Reynolds stress tensor R_{ij} replaced

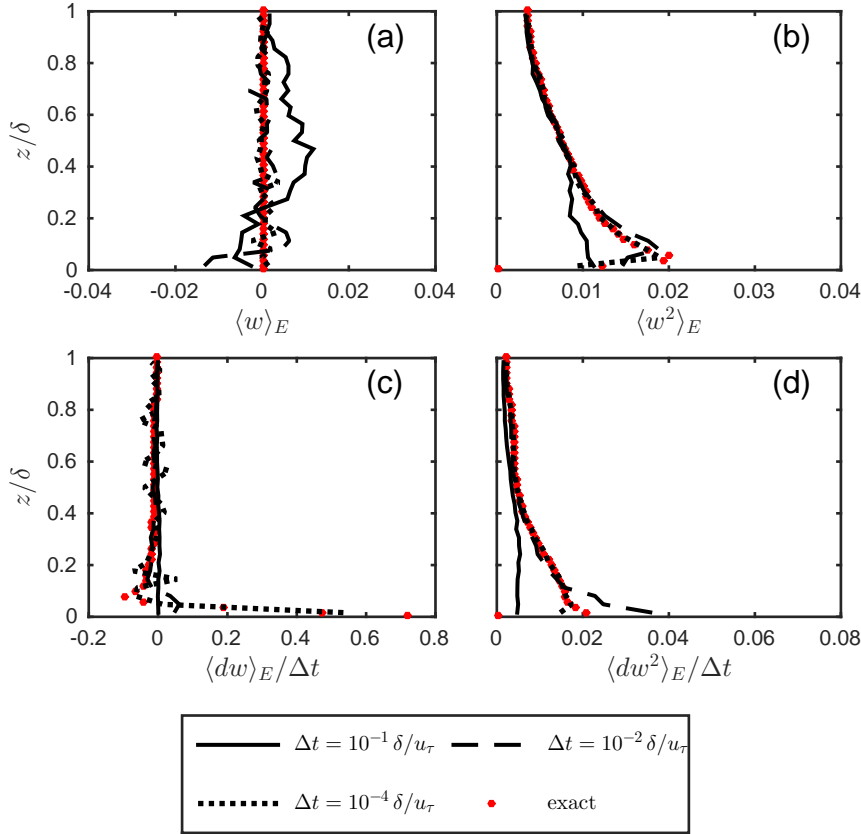


Fig. 10 Eulerian particle velocity statistics for the channel flow test case when an implicit backward Euler integration scheme was used. Calculated profiles are compared to exact profiles for (a) average particle vertical velocity, (b) particle vertical velocity variance, (c) average vertical particle acceleration, (d) variance of particle vertical velocity increments. Profiles are calculated by performing an average or variance over all particles residing in the i^{th} discrete spatial bin.

641 by the subfilter-scale stress tensor τ_{ij} . As in Eq. 15, it is necessary that τ_{ij}
 642 is positive semi-definite and non-singular (realizable). A method is presented
 643 below in Sect. 5.3 to ensure realizability of the stress tensor.

644 The assumed form for P_E can be substituted into the Fokker-Planck equation
 645 in the same way as in the Reynolds-averaged case, which yields an equation
 646 identical to Eq. 16 except with u_i replaced by $u_{s,i}$, R_{ij} replaced by τ_{ij} ,
 647 and ε is an instantaneous and local value. The turbulence dissipation rate ε
 648 represents approximately the same quantity as in Eq. 16 on average. If Δ lies
 649 in the inertial subrange (a critical assumption for most LES models), dissipation
 650 is still unresolved in LES. Thus, the rate at which turbulence is removed
 651 by dissipation should be the same on average in both the Reynolds-averaged

652 and LES approaches. However, the precise value of ε that is chosen is not
 653 critical for the present discussion, as the goal of this work is simply to match
 654 the prescribed distribution of ε , whatever it may be.

655 5.2 Eulerian LES momentum solution

656 A large-eddy simulation was performed for a channel flow to drive the 3D
 657 anisotropic model. The LES model is described in full detail in [Stoll and Porté-
 658 Agel \(2006\)](#), and only essential details are summarized here. As introduced
 659 above, LES resolves turbulent motions with length scales larger than the char-
 660 acteristic grid scale Δ , which for hexahedral grid cells of size $\Delta_x \times \Delta_y \times \Delta_z$, can
 661 be given by $(\Delta_x \Delta_y \Delta_z)^{1/3}$. In essence, this is a generalization of the Reynolds-
 662 averaged approach where *all* turbulent motions are below the filter scale. In
 663 both cases, the effects of the subfilter-scales must be modelled.

664 The deviatoric component of the subfilter-scale stress tensor was modelled
 665 using the Smagorinsky approach

$$\tau_{ij} = \frac{2}{3} k_s \delta_{ij} - 2 (\Delta C_s)^2 |\tilde{S}| \tilde{S}_{ij}, \quad (22)$$

666 where k_s is the subfilter-scale turbulent kinetic energy, $\tilde{S}_{ij} = \frac{1}{2} \left(\frac{\partial \tilde{u}_i}{\partial x_j} + \frac{\partial \tilde{u}_j}{\partial x_i} \right)$ is
 667 the resolved strain rate tensor, and $|\tilde{S}| = \left(2 \tilde{S}_{ij} \tilde{S}_{ij} \right)^{1/2}$. C_s is the Smagorinsky
 668 coefficient, which is scale-dependent and calculated dynamically along fluid
 669 particle trajectories following [Stoll and Porté-Agel \(2006\)](#). Test filtering for
 670 the scale-dependent scheme is performed at scales of 2Δ and 4Δ .

671 The subfilter-scale dissipation rate (needed by the dispersion model) was
 672 calculated following the recommendation of [Meneveau and O'Neil \(1994\)](#), who
 673 suggested the scaling of $\varepsilon \sim k_s |\tilde{S}|$. An initial guess for k_s was calculated using
 674 the model suggested by [Mason and Callen \(1986\)](#) $k_s = \left(\Delta C_s |\tilde{S}| \right)^2 / 0.3$, which
 675 is equivalent to the frequently used model of [Yoshizawa \(1986\)](#) to within a
 676 constant.

677 5.3 Ensuring a realizable stress tensor

678 The anisotropic Lagrangian particle dispersion model requires specification of
 679 the total (i.e., deviatoric plus normal components) of the stress tensor. Many
 680 turbulence models compute the deviatoric and normal components separately,
 681 which means there is no guarantee that the total stress tensor is realizable.

682 In order for τ_{ij} (or R_{ij}) to be realizable, the normal stresses must be large
 683 enough that the three invariants of the tensor are positive (Sagaut, 2002), i.e.,

$$\tau_{kk} > 0, \quad (23a)$$

$$\tau_{11}\tau_{22} + \tau_{11}\tau_{33} + \tau_{22}\tau_{33} - \tau_{12}^2 - \tau_{13}^2 - \tau_{23}^2 > 0, \quad (23b)$$

$$\det(\tau_{ij}) > 0. \quad (23c)$$

684 In practice, it was necessary to ensure that the invariants were larger than some
 685 small positive threshold I_ϵ in order to avoid marginal realizability. It was found
 686 that I_ϵ could not be arbitrarily small. For this test case $I_\epsilon = 10^{-5}$ was sufficient
 687 to eliminate all rogue trajectories. Increasing this value by one or two orders
 688 of magnitude seemed to have no noticeable impact on results. Decreasing by
 689 one or two orders of magnitude resulted in very infrequent occurrence of rogue
 690 trajectories (i.e., less than 10 out of 100,000 total trajectories), which did not
 691 seem to impact results. It is noted that required values of I_ϵ may be flow-
 692 dependent and also dependent on model details.

693 The following methodology was used to find the k_s that ensured a real-
 694 izable stress tensor. k_s was estimated at every Eulerian grid point as $k_s =$
 695 $(\Delta C_s |\tilde{S}|)^2 / 0.3$. The resulting τ_{ij} was then checked that its three invariants
 696 were greater than I_ϵ . If not, k_s was incrementally increased by 5% until the
 697 invariants were all above the threshold. This is not the most efficient algo-
 698 rithm, and if further computational efficiency is desired a faster converging
 699 method could be used such as bisection or the Newton-Raphson method. It
 700 was possible that although τ_{ij} was realizable at every Eulerian grid node,
 701 when interpolated to the particle position it could fail to be realizable, par-
 702 ticularly near the wall. Thus, a similar check (and possibly correction) was
 703 performed to ensure that the interpolated τ_{ij} was still realizable. The addi-
 704 tional computational expense from performing these checks and corrections
 705 was not substantial, as a correction was most commonly only necessary for
 706 particles between the lowest computational grid node and the wall.

707 5.4 Test case set-up

708 LES was performed of a very high Reynolds number channel flow. The test case
 709 was essentially the same as in Porté-Agel et al (2000). The flow was bounded in
 710 the vertical direction by a lower no-slip, rough wall, and an upper zero stress
 711 rigid lid at $z = \delta$. The lower wall had a characteristic roughness length of
 712 $z_0 = 10^{-4} \delta$. Lateral boundaries were periodic. Flow was driven by a spatially
 713 constant horizontal pressure gradient of $F_x = 3.125 \times 10^{-3} u_\tau^2$. The domain of
 714 size $2\pi\delta \times 2\pi\delta \times \delta$ was discretized into $32 \times 32 \times 32$ uniform hexahedral cells,
 715 where δ is the channel half-height. This grid resolution is quite low for this
 716 flow, which was intentionally chosen to emphasize the effects of the unresolved
 717 scales.

718 For simplicity, the Lagrangian dispersion simulations were driven by a single
 719 instantaneous realization of the LES. This was preferable as it resulted in
 720 minimal data that could be easily distributed with the code provided in the
 721 supplementary material. Such a case is physically equivalent to having a flow
 722 with high heterogeneity in space, but that is steady in time, similar to that of a
 723 Reynolds-averaged flow with highly complex geometry. From the point of view
 724 of a particle, the difference between heterogeneity in space and unsteadiness
 725 in time is not likely to be significant, as either one gets wrapped into the total
 726 derivative term in the same way.

727 In the dispersion simulations, 100,000 particles were instantaneously re-
 728 leased from a uniform source, and tracked over a period of $T = \delta u_\tau^{-1}$. Nu-
 729 merical differentiation of Eulerian fields were calculated using a second-order
 730 central finite differencing scheme in the horizontal. In the vertical, a second-
 731 order forward scheme was used except at the top two nodes, where a backward
 732 scheme was used. Rogue trajectories were assumed to occur when $|u_{s,i}| >$
 733 $10 \max(\frac{2}{3}k_s)^{1/2}$ was satisfied for any component of $u_{s,i}$.

734 5.5 Input Profiles

735 For reference, various LES flow profiles are given in Fig. 11, which gives a
 736 sense of the importance of the subfilter-scale model. On average, about 90%
 737 of the *tke* was resolved by the numerical grid. At maximum, the subfilter-scale
 738 *tke* accounted for about 25% of the total *tke*. Note that all variables were
 739 forced to zero at the wall for reasons discussed in the previous test case. This
 740 appears especially abrupt for this test case given that the numerical grid is
 741 quite coarse. As the LES grid is refined, this assumption will improve.

742 5.6 Particle position p.d.f.s and Eulerian profiles

743 Figure 12 shows p.d.f.s of vertical particle position using various schemes.
 744 When an explicit forward Euler scheme was used and no efforts were made
 745 to ensure a realizable τ_{ij} , rogue trajectories became significant (Fig. 12a-c).
 746 By the end of this simulation, roughly 20% of particles were rogue regard-
 747 less of timestep. Surprisingly, the number of rogue trajectories increased with
 748 decreasing timestep.

749 Ensuring that τ_{ij} was realizable significantly decreased the number of
 750 rogue trajectories (Fig. 12d-f). However, even for a very small timestep ($\Delta t =$
 751 $10^{-4} \delta u_\tau^{-1}$), the explicit integration scheme still produced over 100 rogue tra-
 752 jectories. It is likely that the timestep would have to be extremely small to
 753 eliminate all rogue trajectories. As discussed previously, even a small number
 754 of rogue trajectories can be problematic. If the simulation is allowed to run
 755 long enough, there may be a point where enough rogue particles accumulate
 756 that results are noticeably affected.

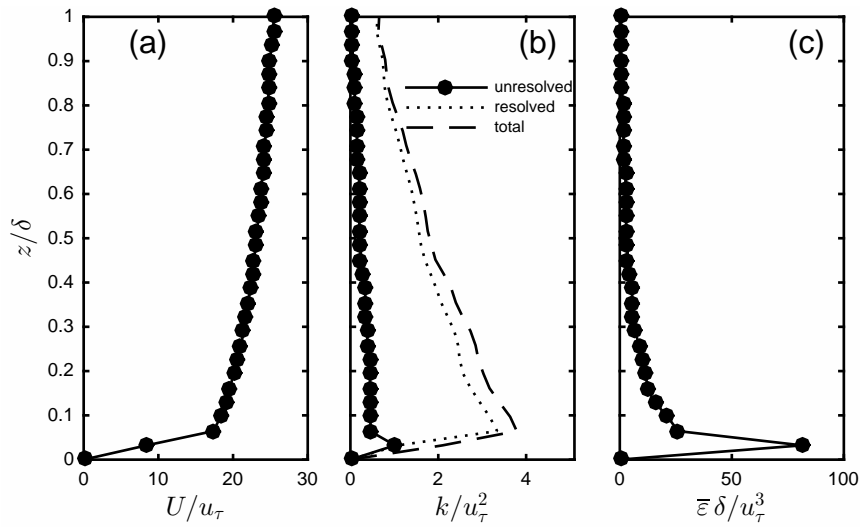


Fig. 11 Eulerian profiles for the LES test case: (a) mean velocity, (b) unresolved, resolved, and total turbulent kinetic energy, (c) viscous dissipation rate. Profiles are formed by averaging in the horizontal at the instant used to drive the simulations.

757 As expected, the implicit backward Euler scheme produced no rogue tra-
 758 jectories, provided that τ_{ij} is realizable. The timestep did not have a significant
 759 effect on the implicit model's ability to satisfy the second law of thermody-
 760 namics. This is likely related to the fact that the resolved velocity (which
 761 clearly satisfies the thermodynamic constraint) accounts for the majority of
 762 the total velocity. When a relatively large timestep was used with the explicit
 763 numerical scheme ($\Delta t = 10^{-2} \delta u_\tau^{-1}$), some un-mixing occurred. The presence
 764 of rogue trajectories could have had some influence on this un-mixing, since
 765 the implicit scheme with an equivalent timestep showed almost no un-mixing.

766 Figure 13 shows Eulerian profiles of particle velocity statistics near the
 767 wall when the implicit integration scheme was used. Well away from the wall,
 768 the model was able to match specified Eulerian profiles regardless of timestep,
 769 which is because gradients are very small in this region. As with previous
 770 test cases, using too large of a timestep meant that Eulerian particle velocity
 771 statistics were under predicted in regions of large gradients (i.e., near the
 772 wall) with respect to the exact profiles specified as inputs. As the timestep was
 773 reduced, particle velocity statistics converged to the exact values. Although not
 774 shown, if an isotropic model were used that neglected off-diagonal components
 775 of τ_{ij} , the model would be able to match profiles of $\langle k_s^2 \rangle$ and $\langle (dw_s)^2 \rangle_E / \Delta t$.
 776 However, all cross-correlations would clearly be zero in that case.

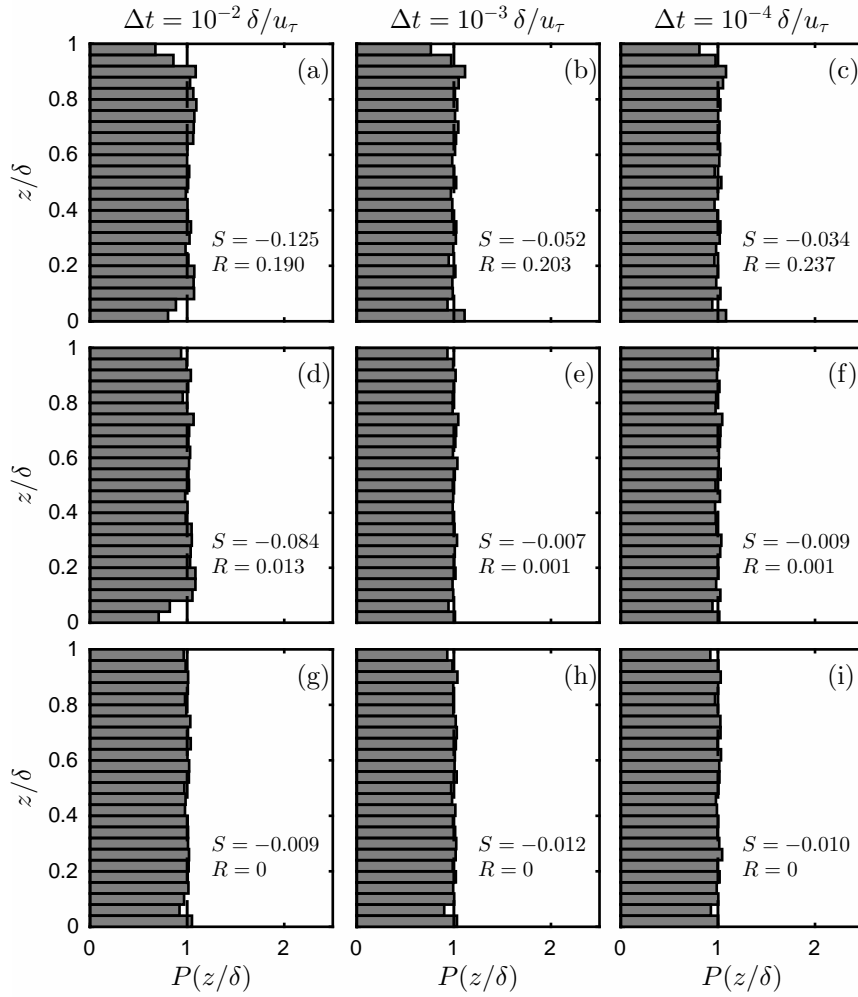


Fig. 12 Probability density functions of particle position for the LES test case with varying timestep (values given in figure). (a)-(c) shows results for the explicit forward Euler scheme without ensuring that τ_{ij} is realizable, (d)-(f) shows results for the explicit forward Euler scheme while ensuring that τ_{ij} is realizable, and (g)-(i) shows results for the implicit backward Euler scheme (with realizable τ_{ij}). R is the fraction of particles that were ‘rogue’, or $|u_{s,i}| > 10 \max(\frac{2}{3}k_s)^{1/2}$, and S is the entropy of the plume.

777 6 Summary

778 This study explored aspects of the numerical solution of Lagrangian stochastic
 779 model equations. Isotropic, Reynolds-averaged models were examined using a
 780 simple sinusoidal turbulence field, as well as using channel flow data. The gen-
 781 eralized three-dimensional and anisotropic model formulations were examined

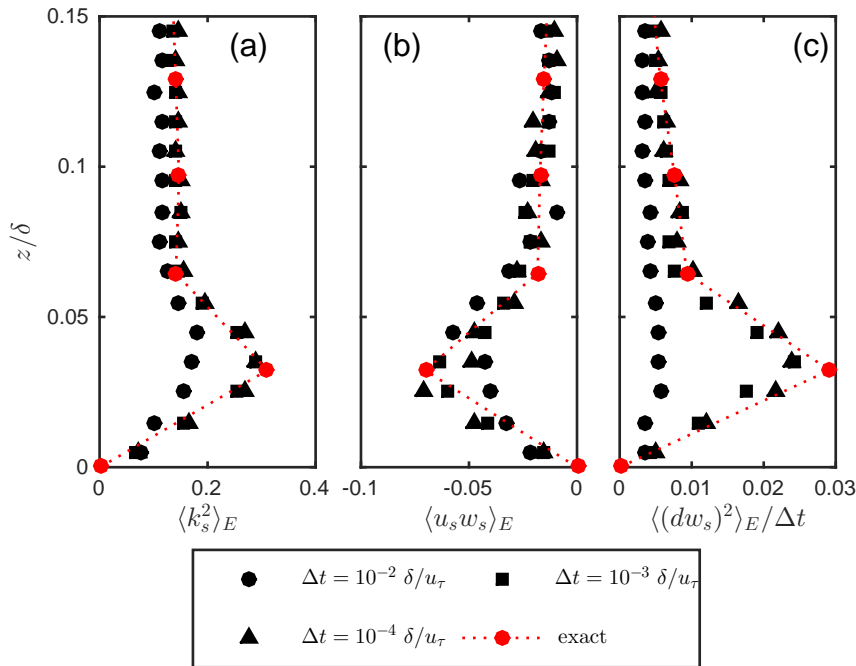


Fig. 13 Eulerian particle velocity profiles for the LES test case with an implicit integration scheme: (a) sub-filter scale turbulent kinetic energy, (b) covariance between u_s and w_s , and (c) variance of vertical velocity increments. Profiles are formed by calculating an average or variance over all particles residing in the i^{th} discrete spatial bin.

782 using large-eddy simulations, although the results are directly applicable to
 783 Reynolds-averaged models as well.

784 It was found that the so-called rogue trajectories result from numerical
 785 instability of the temporal integration scheme. Due to the stiff nature of the
 786 velocity evolution equations, very small timesteps are required to maintain
 787 stability when an explicit scheme is used. A natural remedy for this problem
 788 is to use an implicit numerical scheme. Formulating a fully implicit scheme is
 789 complicated by the fact that the velocity evolution equation is coupled with the
 790 position evolution equation, and by the nonlinearity of the velocity evolution
 791 equation. Furthermore, in the case of three-dimensional, anisotropic turbu-
 792 lence, the three components of the velocity evolution equation are nonlinearly
 793 coupled. To solve these problems, the equations were linearized by re-writing
 794 the total derivative term using the Lagrangian definition. Furthermore, coeffi-
 795 cients were ‘lagged’ in order to avoid having to use a costly iterative scheme.
 796 The resulting implicit scheme was shown to be unconditionally stable. In the
 797 case of the anisotropic model, it was critical that the velocity covariance tensor
 798 be realizable, otherwise rogue trajectories frequently occurred regardless of the
 799 size of the timestep. Realizability was enforced by ensuring that the turbulent

800 kinetic energy was large enough that the three tensor invariants were larger
801 than some specified threshold.

802 In addition to examining stability, the degree to which statistics of the
803 numerical solution matched the specified inputs was examined. Fortunately,
804 the exact statistics of the solution are always known, since they are simply
805 given by model inputs. The fundamental task of the numerical solution is
806 to provide an ensemble of particles whose Eulerian velocity statistics match
807 those that were originally specified. As expected, it was found that the size
808 of the chosen timestep determined the degree to which computed particle
809 statistics matched specified statistics. In addition to failing to match specified
810 statistics, using too large of a timestep also induced a mean particle flux that
811 leads to a violation of the well-mixed condition. If the timestep is extremely
812 large, it was found that the well-mixed condition could also be satisfied, but
813 that Eulerian particle statistics would be incorrect. Thus, it was recommended
814 that numerical solutions be verified by comparing computed Eulerian velocity
815 statistics with those specified as inputs.

816 No scenarios were found where it was preferable to use an explicit scheme
817 over an implicit scheme. When the timestep required for stability of the explicit
818 scheme is unfeasibly small, the implicit scheme is preferable because it can pro-
819 vide reasonable results with a much larger timestep than the explicit scheme.
820 When the anisotropic model is used, there is a small additional cost associated
821 with the inversion of a 3×3 matrix which results from the implicit formula-
822 tion. However, this seems minor compared to the added assurance of obtaining
823 an unconditionally stable scheme. Furthermore, for moderate timesteps, the
824 implicit scheme showed better overall performance than the explicit scheme.
825 Thus, it is recommended to always use the implicit scheme.

826 Although only Gaussian models were examined, future work should ex-
827 plore the use of implicit numerical schemes for cases of skewed turbulence
828 (e.g., [Luhar and Britter, 1989](#); [Weil, 1990](#)). Skewed models present significant
829 challenges, as the model equations themselves are not algebraically explicit.
830 As such, formulation of an implicit numerical scheme will almost certainly
831 involve an iterative approach. This will create a noticeable increase in compu-
832 tational cost, which may or may not be acceptable given the severity of rogue
833 trajectories. Regardless, many of the results presented herein will likely still
834 apply, such as the importance of numerical accuracy in satisfying the WMC
835 and matching prescribed Eulerian velocity p.d.f.s.

836 **Acknowledgements** The author wishes to acknowledge fruitful discussions with Drs. Rob
837 Stoll and Eric Pardyjak in formulating the ideas presented in this work. This research was
838 supported by U.S. National Science Foundation grants IDR CBET-PDM 113458 and AGS
839 1255662, and United States Department of Agriculture (USDA) project 5358-22000-039-
840 00D. The use, trade, firm, or corporation names in this publication are for information and
841 convenience of the reader. Such use does not constitute an endorsement or approval by the
842 USDA or the Agricultural Research Service of any product or service to the exclusion of
843 others that may be suitable.

References

- 844 **References**
- 845 Bailey BN, Stoll R, Pardyjak ER, Mahaffee WF (2014) Effect of canopy archi-
846 tecture on vertical transport of massless particles. *Atmos Env* 95:480–489
- 847 Du S (1997) Universality of the Lagrangian velocity structure function con-
848 stant (C_0) across different kinds of turbulence. *Bound-Layer Meteorol* 83:207–
849 219
- 850 Du Vachat R (1977) Realizability inequalities in turbulent flows. *Phys Fluids*
851 20:551–556
- 852 Hairer E, Wanner G (1996) *Solving Ordinary Differential Equations II: Stiff*
853 *and Differential-Algebraic Problems*, 2nd edn. Springer, Berlin Heidelberg,
854 614 pp.
- 855 Kim J, Moin P, Moser R (1987) Turbulence statistics in fully developed channel
856 flow at low Reynolds number. *J Fluid Mech* 177:133–166
- 857 Kloeden PE, Platen E (1992) Higher-order implicit strong numerical schemes
858 for stochastic differential equations. *J Stat Phys* 66:283–314
- 859 Lamba H (2003) An adaptive timestepping algorithm for stochastic differential
860 equations. *J Comp Appl Math* 161:417–430
- 861 Langevin P (1908) Sur la théorie du mouvement Brownien. *C R Acad Sci*
862 (Paris) 146:530–533
- 863 Legg BJ, Raupach MR (1982) Markov-chain simulation of particle dispersion
864 in inhomogeneous flows: the mean drift velocity induced by a gradient in
865 Eulerian velocity variance. *Bound-Layer Meteorol* 24:3–13
- 866 Leveque RJ (2007) *Finite Difference Methods for Ordinary and Partial Differ-*
867 *ential Equations: Steady-State and Time-Dependent Problems*. Society for
868 Industrial and Applied Mathematics, Philadelphia, PA
- 869 Lin J, Brunner D, Gerbig C, Stohl A, Luhar A, Webley P (eds) (2013) *La-*
870 *grangian Modeling of the Atmosphere*. American Geophysical Union, Wash-
871 ington, DC, 349 pp.
- 872 Lin JC (2013) How can we satisfy the well-mixed criterion in highly inhomoge-
873 nous flows? a practical approach. In: Lin J, Brunner D, Gerbig C, Stohl A,
874 Luhar A, Webley P (eds) *Lagrangian Modeling of the Atmosphere*, Ameri-
875 can Geophysical Union, Washington, DC, pp 59–69
- 876 Luhar AK, Britter RE (1989) A random walk model for dispersion in inhomo-
877 geneous turbulence in a convective boundary layer. *Atmos Env* 23:1911–1924
- 878 Mansour NN, Kim J, Moin P (1988) Reynolds-stress and dissipation-rate bud-
879 gets in a turbulent channel flow. *J Fluid Mech* 194:15–44
- 880 Mason PJ, Callen NS (1986) On the magnitude of the subgrid-scale eddy
881 coefficient in large-eddy simulations of turbulent channel flow. *J Fluid Mech*
882 162:439–462
- 883 Mauthner S (1998) Step size control in the numerical solution of stochastic
884 differential equations. *J Comp Appl Math* 100:93–109
- 885 Meneveau C, O’Neil J (1994) Scaling laws of the dissipation rate of turbulent
886 subgrid-scale kinetic energy. *Phys Rev E* 49:2866–2874
- 887 Pope SB (1987) Consistency conditions for randomwalk models of turbulent
888 dispersion. *Phys Fluids* 30:2374–2379

- 889 Porté-Agel F, Meneveau C, Parlange MB (2000) A scale-dependent dynamic
890 model for large-eddy simulations: Application to a neutral atmospheric
891 boundary layer. *J Fluid Mech* 415:261–284
- 892 Postma JV (2015) Timestep buffering to preserve the well-mixed condition in
893 Lagrangian stochastic simulations. *Bound-Layer Meteorol* 156:15–36
- 894 Postma JV, Yee E, Wilson JD (2012) First-order inconsistencies caused by
895 rogue trajectories. *Boundary-Layer Meteorol* 144:431–439
- 896 Press WH, Teukolsky SA, Vetterling WT, Flannery BP (2007) *Numerical
897 Recipes: The Art of Scientific Computing*. Cambridge University Press,
898 Cambridge, U.K., 1256 pp.
- 899 Rodean HC (1991) The universal constant for the Lagrangian structure func-
900 tion. *Phys Fluids A* 3:1479–1480
- 901 Rodean HC (1996) *Stochastic Lagrangian Models of Turbulent Diffusion*.
902 Amer. Meteor. Soc., Boston, MA, 84 pp.
- 903 Sagaut P (2002) *Large Eddy Simulation for Incompressible flows: An Intro-
904 duction*, 3rd edn. Springer-Verlag, Berlin Heidelberg, 585 pp.
- 905 Sawford BL (1986) Generalized random forcing in randomwalk turbulent dis-
906 persion models. *Phys Fluids* 29:3582
- 907 Schumann U (1977) Realizability of Reynolds-stress turbulence models. *Phys
908 Fluids* 20:721–725
- 909 Stoll R, Porté-Agel F (2006) Dynamic subgrid-scale models for momentum
910 and scalar fluxes in large-eddy simulations of neutrally stratified atmo-
911 spheric boundary layers over heterogeneous terrain. *Water Resources Res*
912 42:W01,409
- 913 Thomson DJ (1984) Random walk modelling of diffusion in inhomogeneous
914 turbulence. *Quart J R Met Soc* 110:1107–1120
- 915 Thomson DJ (1987) Criteria for the selection of stochastic models of particle
916 trajectories in turbulent flows. *J Fluid Mech* 180:529–556
- 917 Weil JC (1990) A diagnosis of the asymmetry in top-down and bottom-up
918 diffusion using a Lagrangian stochastic model. *J Atmos Sci* 47:501–515
- 919 Wilson JD (2013) “Rogue velocities” in a Lagrangian stochastic model for ide-
920 alized inhomogeneous turbulence. In: Lin J, Brunner D, Gerbig C, Stohl A,
921 Luhar A, Webley P (eds) *Lagrangian Modeling of the Atmosphere*, Ameri-
922 can Geophysical Union, Washington, DC, pp 53–57
- 923 Wilson JD, Thurtell GW, Kidd GE (1981) Numerical simulation of particle
924 trajectories in inhomogeneous turbulence, II: Systems with variable turbu-
925 lent velocity scale. *Bound-Layer Meteorol* 21:423–441
- 926 Yee E, Wilson JD (2007) Instability in Lagrangian stochastic trajectory mod-
927 els, and a method for its cure. *Boundary-Layer Meteorol* 122:243–261
- 928 Yoshizawa A (1986) Statistical theory for compressible turbulent shear flows,
929 with the application to subgrid modeling. *Phys Fluids* 29:2152